Modeling multicrack propagation by the fast multipole symmetric Galerkin BEM

Anicet Dansou, Saida Mouhoubi, Cyrille Chazallon, Marc Bonnet

Modeling multicrack propagation by the Fast Multipole Symmetric Galerkin BEM

Anicet Dansou[a], Saïda Mouhoubi[a], Cyrille Chazallon[a], Marc Bonnet[b]

[a]*ICube, UMR 7357, CNRS, University of Strasbourg*
INSA Strasbourg, 24 bd de la victoire, 67084 Strasbourg Cedex, France
anicet.dansou@insa-strasbourg.fr, saida.mouhoubi@insa-strasbourg.fr, cyrille.chazallon@insa-strasbourg.fr

[b]*POEMS (CNRS, INRIA, ENSTA), ENSTA, 828 boulevard des Maréchaux, 91120 Palaiseau, France.*
mbonnet@ensta.fr

Abstract

The Fast Multipole Method coupled with the Symmetric Galerkin BEM is employed in this work to simulate fatigue crack growth. The resulted crack propagation code is accelerated with a fast matrix update, a parallel implementation and a sparse matrix format. By using multiple nodes, this code accommodates also multiple surface-breaking cracks. The numerical tests presented herein allow the propagation of multiple cracks in single or multilayer domains.

Keywords: *SGBEM, FMM, multizone, multicrack, crack propagation*

1. Introduction

Despite the general prominence and versatility of the FEM in many application areas of science and engineering, configurations characteristics such as unbounded media or crack propagation are factors making the BEM very effective and efficient. In fracture mechanics, high mesh density is needed for the FEM to accurately compute the Stress intensity factors (SIFs) or the energy release rate to simulate the crack growth. Also, the simulation of crack propagation entails demanding and labor-intensive repeated domain remeshing [1]. The BEM-based approaches, on the other hand, are well suited for linear elastic fracture mechanics for several reasons: (i) the dimension reduction leads to simpler data preparation; (ii) the remeshing task is more straightforward than for the FEM, even for 3D geometries, since only the crack surfaces need remeshing during the crack growth; (iii) stresses ahead of cracks and other singularities can be computed accurately. Many developments have been devoted to improve the ability of the BEM in crack propagation simulation. Li and Keer [2] model the growth in shear mode of a crack embedded in an unbounded medium. Mi and Aliabadi [3] and Mi [4] adopted the dual approach to enforce the traction equation in addition to the traditional Somigliana displacement identity at points of the fracture surface, an approach that puts constraints on BEM discretization by requiring C^1 smoothness of the displacement field at the collocation points.

The symmetric Galerkin version of the BEM (SGBEM) has further advantages. It produces a symmetric coefficient matrix (see e.g. Yoshida et al. [5] or Frangi et al. [6] for crack problems), a feature that halves the computational and memory costs when using direct solvers and facilitates BEM/FEM coupling [7, 8, 9]. Moreover, the variational framework underlying the SGBEM permits mathematical analysis of e.g. the well-posedness of the continuous problem and the convergence of discretization schemes [10, 11]. For fractured domains where cracks are treated as loci of displacement discontinuities, the symmetry property still holds provided the unknowns on the crack

surfaces are the displacement jumps $\boldsymbol{\phi} := \boldsymbol{u}^+ - \boldsymbol{u}^-$. Another advantage of the SGBEM over the traditional collocation BEM for crack problems is that all integral operators of the SGBEM, even the hypersingular ones, can be treated using standard C^0 boundary element interpolations. For this reason, the SGBEM can easily model the crack tip behavior and provide smoother solutions in the vicinity of geometric discontinuities. Frangi [12] applied the SGBEM to a simple case of fatigue crack growth. Similar methods were proposed by Roberts et al. [13], and Kitey et al. [14] for modeling crack growth in particulate composites. Xu et al. [15] applied the SGBEM to investigate 2D crack propagation, while Tavara modeled cohesive crack growth in homogeneous media [16].

Over recent decades, the performance of boundary analysis is further improved with the advent of the Fast Multipole Method (FMM) [17] and other acceleration methodologies. The classical bottlenecks of the BEMs caused by the fully-populated matrix are alleviated as the FMM splits all element integrals into *near-field* and *far-field* interactions, the latter being clustered in a recursive, multilevel fashion. This process results in (i) a lessened storage complexity, typically defined by the sparse *near-field* matrix, and (ii) faster solution based on iterative solvers (complexity of order $O(N)$ instead of $O(N^2)$ per iteration, N being the number of BEM unknowns). This makes boundary element analysis applicable with very good performance to large BEM models (see e.g. the application of FMM to elastodynamics [18]).

In this work, the FM-SGBEM treatment of cracked three-dimensional elastostatic media previously presented in [19] is extended to the simulation of fatigue crack growth. The adopted fatigue propagation criterion is the commonly-used [12, 3, 20, 21] Paris law. The FM-SGBEM formulation for cracked domains is summarized in Sec. 2. The main aspects of the crack propagation algorithm are then presented in Sec. 3. Section 4 is then devoted to several method enhancements. Finally, Sections 5 and 6 report numerical experiments featuring, respectively, stationary or propagating multiple cracks in homogeneous or piece-wise homogeneous domain.

2. Fast multipole symmetric Galerkin BEM

2.1. Symmetric Galerkin BEM

Consider a fractured elastic solid Ω subjected to prescribed tractions $\boldsymbol{t}^D$ on the boundary S_t and displacement constraints $\boldsymbol{u}^D$ on S_u (Fig. 1). The boundary of Ω (including the crack S_c) is thus defined as $S = S_t \cup S_u \cup S_c$. The crack surface S_c supports a displacement discontinuity $\boldsymbol{\phi}$, usually referred to as the crack opening displacement (COD) and defined as

$$\boldsymbol{\phi}(\boldsymbol{x}) = \boldsymbol{u}(\boldsymbol{x}^+) - \boldsymbol{u}(\boldsymbol{x}^-),$$
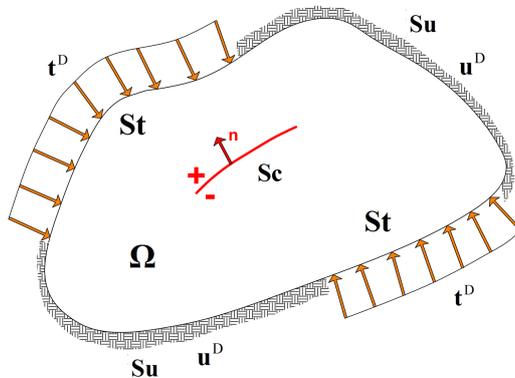
Figure 1: *Solid containing a crack: notation*

2

where $\boldsymbol{u}^+(\boldsymbol{x})$ and $\boldsymbol{u}^-(\boldsymbol{x})$ are the traces of $\boldsymbol{u}$ on the upper and lower sides of S_c (the unit normal to S_c pointing by convention from the lower to the upper side). Details of the mathematical developments of the SGBEM can be found in many references, e.g. [22, 10]. The variational boundary integral formulation for the cracked elastic solid is written as: find $\boldsymbol{u} \in \mathcal{V}_u, \ \boldsymbol{\phi} \in \mathcal{V}_c, \ \boldsymbol{t} \in \mathcal{V}_t$ such that

$$
\left.\begin{aligned}
\mathcal{B}_{uu}(\boldsymbol{u}, \widetilde{\boldsymbol{u}}) + \mathcal{B}_{tu}(\boldsymbol{t}, \widetilde{\boldsymbol{u}}) + \mathcal{B}_{cu}(\boldsymbol{\phi}, \widetilde{\boldsymbol{u}}) = \mathcal{F}_u(\widetilde{\boldsymbol{u}}) \\
\mathcal{B}_{ut}(\boldsymbol{u}, \widetilde{\boldsymbol{t}}) + \mathcal{B}_{tt}(\boldsymbol{t}, \widetilde{\boldsymbol{t}}) + \mathcal{B}_{ct}(\boldsymbol{\phi}, \widetilde{\boldsymbol{t}}) = \mathcal{F}_t(\widetilde{\boldsymbol{t}}) \\
\mathcal{B}_{uc}(\boldsymbol{u}, \widetilde{\boldsymbol{\phi}}) + \mathcal{B}_{tc}(\boldsymbol{t}, \widetilde{\boldsymbol{\phi}}) + \mathcal{B}_{cc}(\boldsymbol{\phi}, \widetilde{\boldsymbol{\phi}}) = \mathcal{F}_c(\widetilde{\boldsymbol{\phi}})
\end{aligned}\right\} \qquad \text{for all } \widetilde{\boldsymbol{u}} \in \mathcal{V}_u, \widetilde{\boldsymbol{\phi}} \in \mathcal{V}_c, \widetilde{\boldsymbol{t}} \in \mathcal{V}_t \qquad (1)
$$

The bilinear forms $\mathcal{B}_{uu}$ etc. and linear functionals $\mathcal{F}_u$ are usual integral operators written in weak form. Their explicit expressions are provided in [23, 24]. For example, we have

$$
\mathcal{B}_{tt}(\boldsymbol{t}, \widetilde{\boldsymbol{t}}) = \int_{S_u} \int_{S_u} t_k(\boldsymbol{x}) U_i^k(\boldsymbol{x}, \widetilde{\boldsymbol{x}}) \widetilde{t}_i(\widetilde{\boldsymbol{x}}) dS_{\tilde{x}} dS_x
$$

$$
\mathcal{B}_{tu}(\boldsymbol{t}, \widetilde{\boldsymbol{u}}) = -\int_{S_u} \int_{S_T} t_k(\boldsymbol{x}) T_i^k(\boldsymbol{x}, \widetilde{\boldsymbol{x}}) \widetilde{u}_i(\widetilde{\boldsymbol{x}}) dS_{\tilde{x}} dS_x \qquad (2)
$$

$$
\mathcal{B}_{\phi\phi}(\boldsymbol{\phi}, \widetilde{\boldsymbol{\phi}}) = \int_{S_c} \int_{S_c} [R\phi]_{iq}(\boldsymbol{x}) B_{ikqs}(\boldsymbol{r}) [R\tilde{\phi}]_{ks}(\widetilde{\boldsymbol{x}}) dS_{\tilde{x}} dS_x
$$

where the unknowns $\boldsymbol{u}, \boldsymbol{t}$ and $\boldsymbol{\phi}$ have respective supports S_t, S_u and S_c; $U_i^k(\boldsymbol{x}, \widetilde{\boldsymbol{x}})$ and $T_i^k(\boldsymbol{x}, \widetilde{\boldsymbol{x}})$ are the ith component of the Kelvin fundamental displacement and traction, respectively, at $\boldsymbol{x} \in \mathbb{R}^3$ created by a point force applied at $\widetilde{\boldsymbol{x}} \in \mathbb{R}^3$ along the kth coordinate direction, given by

$$
U_i^k(\boldsymbol{x}, \widetilde{\boldsymbol{x}}) = \frac{1}{16\pi\mu(1-\nu)r} [\hat{r}_i \hat{r}_k (3 - 4\nu) + \delta_{ik}]
$$

$$
T_i^k(\boldsymbol{x}, \widetilde{\boldsymbol{x}}) = -\frac{1}{8\pi(1-\nu)r^2} n_j(\boldsymbol{x}) [3\hat{r}_i \hat{r}_k \hat{r}_j + (1 - 2\nu)(\delta_{ik}\hat{r}_j + \delta_{jk}\hat{r}_i - \delta_{ij}\hat{r}_k)]
$$

having set $\boldsymbol{r} = \boldsymbol{x} - \widetilde{\boldsymbol{x}}$, $r = \|\boldsymbol{r}\|$, $\hat{\boldsymbol{r}} = \boldsymbol{r}/r$. The bilinear forms (2) are all defined in terms of $O(r^{-1})$ weakly singular kernels, following a preliminary regularization based on the Stokes theorem together and indirect regularization [25]. The surface curl operator R arises as a result of this manipulation and is defined as:

$$
[Ru]_{ks}(\widetilde{\boldsymbol{x}}) = e_{jfs} n_j u_{k,f}(\widetilde{\boldsymbol{x}})
$$

while the weakly singular fourth-order tensor $\boldsymbol{B}$ is given in component form by

$$
B_{ikqs}(\boldsymbol{r}) = \frac{1}{8\pi(1-\nu)r} [2\delta_{qs}\hat{r}_i \hat{r}_k + 2(\delta_{ik}\delta_{qs} - 2\nu\delta_{is}\delta_{kq} - (1-\nu)\delta_{iq}\delta_{ks})]
$$

The function spaces in problem (1) can be taken as $\mathcal{V}_u = \tilde{H}^{1/2}(S_u; \mathbb{R}^3)$, $\mathcal{V}_c = \tilde{H}^{1/2}(S_c; \mathbb{R}^3)$, $\mathcal{V}_t = H^{-1/2}(S_t; \mathbb{R}^3)$ in terms of Sobolev spaces of fractional index whose definition is given in e.g. [11]. The associated test functions $\widetilde{\boldsymbol{u}}, \widetilde{\boldsymbol{\phi}}, \widetilde{\boldsymbol{t}}$ belong to the same spaces. To implement Galerkin discretizations of problem (1), natural finite-dimensional subspaces of $\mathcal{V}_u, \mathcal{V}_c$ are provided by continuous interpolations of $\boldsymbol{u}$ over S_t and $\boldsymbol{\phi}$ over S_c (with a zero trace on the edges ∂S_t, ∂S_c), while piecewise-continuous interpolation of $\boldsymbol{t}$ over S_u is sufficient for defining appropriate subspaces of $\mathcal{V}_t$ [10]. The SGBEM can therefore approximate all integral operators with standard boundary element interpolations, whereas collocation methods for cracks put more severe constraints on the discretization options. The system of discretized equations arising from (1) is symmetric, and has the form

$$
\mathbf{K}.\mathbf{X} = \mathbf{F} \qquad (3)
$$

3

where $\mathbf{X} \in \mathbb{R}^N$ collects all unknown degrees of freedom (DOFs) on S_t, S_c and S_u while the matrix $\mathbf{K} \in \mathbb{R}^{N \times N}_{\mathrm{sym}}$ and the vector $\mathbf{F} \in \mathbb{R}^N$ result from discretizing the bilinear forms and the linear functionals, respectively, of the entering problem (1). All these features make SGBEM superior to the collocation approach. The matrix $\mathbf{K}$ is, however, fully populated (albeit symmetric), which places a practical limit of $N = O(10^4)$ on the size of SGBEM models solvable on ordinary computers, the computing work and memory required both becoming excessive otherwise.

2.2. Fast multipole method

The fast multipole method (FMM), introduced in [17], aims at improving the performance of boundary element analyses by avoiding the need to evaluate the kernel functions anew for each pair of boundary points encountered. The FMM avoids such repetitions by introducing poles $\boldsymbol{x}_0, \widetilde{\boldsymbol{x}}_0$ (Fig. 2) at which contributions of clusters of points are gathered. It rests on (i) decomposing the relative position vector $\boldsymbol{r} := \boldsymbol{x} - \widetilde{\boldsymbol{x}}$ as $\boldsymbol{r} = \boldsymbol{x}' + \boldsymbol{r}_0 - \widetilde{\boldsymbol{x}}'$ (Fig. 2) and (ii) reformulating the kernel functions as truncated series of products of functions of the local position vectors $\boldsymbol{x}', \widetilde{\boldsymbol{x}}'$. The cluster-wise treatment of contributions to integral operators is only valid for well-separated clusters. This motivates a recursive definition of such clusters using an octree-based partition of the space (smaller but nearer clusters becoming eligible to multipole expansions), which is the essence of the *multi-level* FMM used here (see Fig. 3 for a schematic description). The multi-level
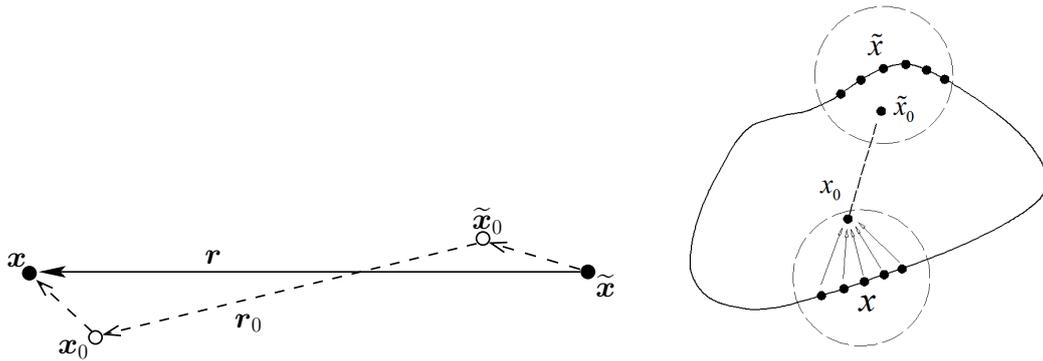
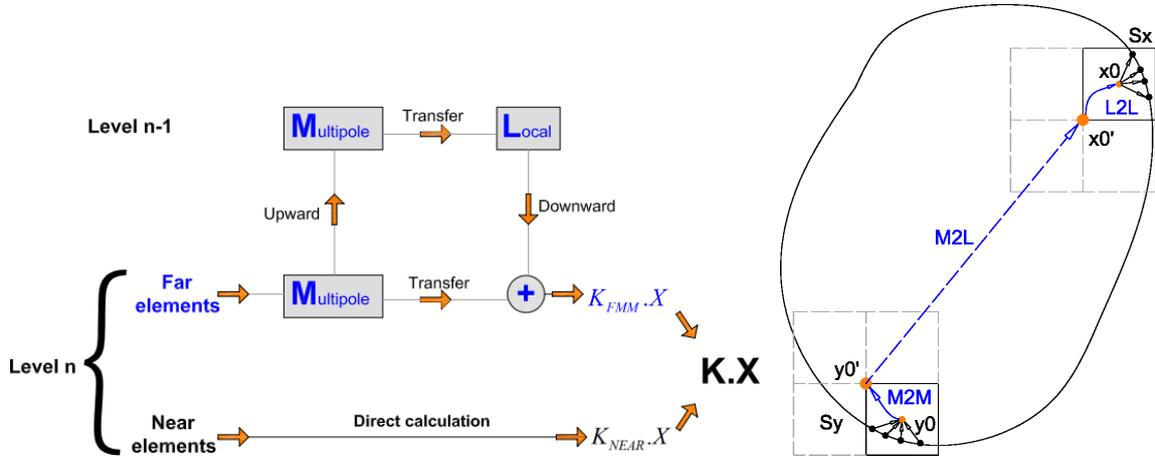**Figure 2:** *Decomposition of the position vector (left); Interactions by FMM scheme (right)*

Figure 3: *Two-level multipole algorithm (left); Multipole operations M2M, M2L and L2L (right)*

4

elastostatic FMM enjoys as a result a $O(N)$ computational complexity. The FMM implicitly splits the SGBEM matrix $\mathbf{K}$ into $\mathbf{K} = \mathbf{K}_{\text{near}} + \mathbf{K}_{\text{FMM}}$, where $\mathbf{K}_{\text{FMM}}$ gathers the contributions arising from multipole expansions and $\mathbf{K}_{\text{near}}$ the close-range influence coefficients that have to be computed by traditional BEM quadrature. The matrix $\mathbf{K}_{\text{FMM}}$ is of course not actually set up; rather, the FMM evaluates products $\mathbf{K}_{\text{FMM}}.\mathbf{X}$ that are used by an iterative solver (usually GMRES) applied to (3). Details of the FMM applied to elastostatic BIEs can be found in e.g. [5, 23].

3. Crack propagation implementation

3.1. Evaluation of stress intensity factors

Several works are devoted to the SIFs, see for example Rooke's Compendium [26] or [27]. The strain and elastic stress fields are singular along the crack front. We use the classical approach based on quarter-point elements along the crack front [28] in order to better capture the behavior near the crack front (see Fig. 4). The SIFs are hence evaluated through extrapolation from the displacement discontinuity field expressed in a local coordinate system $(\boldsymbol{\nu}(s), \boldsymbol{n}(s), \boldsymbol{t}(s))$. For example K_{I} is evaluated [22, 23] by

$$K_{\text{I}}^2 = \frac{\mu}{8(1-\nu)}\sqrt{\frac{2\pi}{a}}\left(4\boldsymbol{\phi}^5 - \boldsymbol{\phi}^1\right) \cdot \boldsymbol{n} \tag{4}$$

where K_{I}^2 is the mode I SIF at the node 2, $\boldsymbol{\phi}^1, \boldsymbol{\phi}^5$ are the nodal CODs at nodes 1 and 5, the nodes being numbered as shown in Fig. 4.

One can alternatively use only the COD value at the quarter-point node, whereby K_{I} at the node 2 is evaluated as

$$K_{\text{I}}^2 = \frac{\mu}{4(1-\nu)}\sqrt{\frac{2\pi}{a}}\boldsymbol{\phi}^5 \cdot \boldsymbol{n}. \tag{5}$$

3.2. Propagation Criterion

Suitable criteria for crack propagation are still being debated, especially for 3D configurations. A simple criterion for fatigue crack growth is the Paris law [29]. Many other propagation criteria
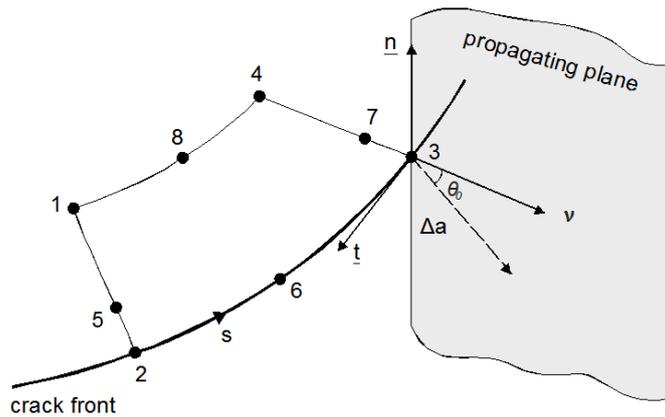

Figure 4: *Quarter-point element at the crack front. Vectors $\boldsymbol{\nu}, \boldsymbol{n}, \boldsymbol{t}$ constitute the local coordinate frame at node **3**. Their directions respectively correpond to the opening, sliding and tearing local modes of fracture propagation.*

are proposed, see e.g. [3, 30, 31, 32, 33]. Paris postulated that sub-critical crack growth under fatigue loading can be predicted in terms of the ranges of stress intensity factors (SIFs) in the same way that thresholds on SIFs or energy release rate characterize brittle fracture. Abundant experimental evidence supports the view that the crack growth rate can be correlated with the cyclic variation in the SIFs, e.g. through

$$\frac{\mathrm{d}a}{\mathrm{d}N}(s) = A\Delta K^m(s) \tag{6}$$

where s is the arc length coordinate along the crack front ∂S_c, N is the current number of loading cycles, $\mathrm{d}a/\mathrm{d}N$ is the fatigue crack advancement rate per cycle, $\Delta K(s) = K^{\max}(s) - K^{\min}(s)$ is the SIF range for the current cycle, while A and m are parameters that depend on the material, environment, frequency, temperature and stress ratio.

The local configuration of the crack front described as in Fig. 4. The geometrical advance of the crack is described by moving points of the crack front in the local $(\boldsymbol{\nu}(s), \boldsymbol{n}(s))$ plane orthogonal to the front. The direction and length of the local crack advancement are represented respectively by the angle $\theta_0(s)$ and the step $\Delta a(s)$. The angle $\theta_0(s)$ is assumed to be given by the maximum circumferential stress criterion [12, 34]

$$\tan\frac{\theta_0}{2} = \frac{1}{4}\left(\frac{K_{\mathrm{Ieff}}}{K_{\mathrm{II}}} - \mathrm{sign}(K_{\mathrm{II}})\sqrt{\left(\frac{K_{\mathrm{Ieff}}}{K_{\mathrm{II}}}\right)^2 + 8}\right),$$

where $K_{\mathrm{Ieff}} = K_{\mathrm{I}} + B|K_{\mathrm{III}}|$ is an "effective" or "equivalent" local mode I stress intensity factor which accounts for the tearing mode being active ($K_{\mathrm{III}} \neq 0$), B being a material parameter. The local geometrical advancement Δa along $\cos\theta_0(s)\boldsymbol{\nu} + \sin\theta_0\boldsymbol{n}$ is determined from the Paris law (6):

$$\Delta a(s) = A\big(\Delta K_{\mathrm{I}}^2(s) + \Delta K_{\mathrm{II}}^2(s)\big)^{m/2}\Delta N.$$

3.3. Propagation algorithm

The algorithm for fatigue crack growth is incremental, the task of each step being to predict the crack growth induced relative to the current configuration by a new sequence of ΔN loading cycles. For each increment, the SGBEM analysis is first performed on the current configuration. The resulting CODs are then used to determine, through the evaluation of corresponding SIFs, the local propagation angle θ_0. At this point, treating the Paris law in explicit fashion, two possibilities arise: either (i) set ΔN and deduce Δa or (ii) set Δa and deduce ΔN. Choice (i) may produce a too-large crack increment Δa if ΔN is inappropriately set, leading to numerical inaccuracies and significant remeshing work. We thus prefer to follow the approach (ii), by fixing *a priori* the maximum propagation length $\Delta a^{\max}$, finding the node(s) where $\Delta K(s)$ is largest, evaluating the corresponding ΔN from (6) at that node, and then computing the extensions $\Delta a(s^i)$ by applying (6) at all crack front nodal positions s^i. The obtained values of $\theta_0(s^i)$ and $\Delta a(s^i)$ are then used to define a row of new quarter-point elements extending the current crack. At crack front nodes s^i shared by two elements, quantities such as $\theta_0(s^i)$ relative to each element may not coincide exactly due to the discontinuity of $\boldsymbol{\nu}$ at $s = s^i$; in such cases, the adjacent values are averaged. The quarter-points of formerly-frontal elements are moved to the middle of the element side while the crack mesh is updated by adding a row of quarter-point elements. The incremental process is repeated until the final number of loading cycles is reached.
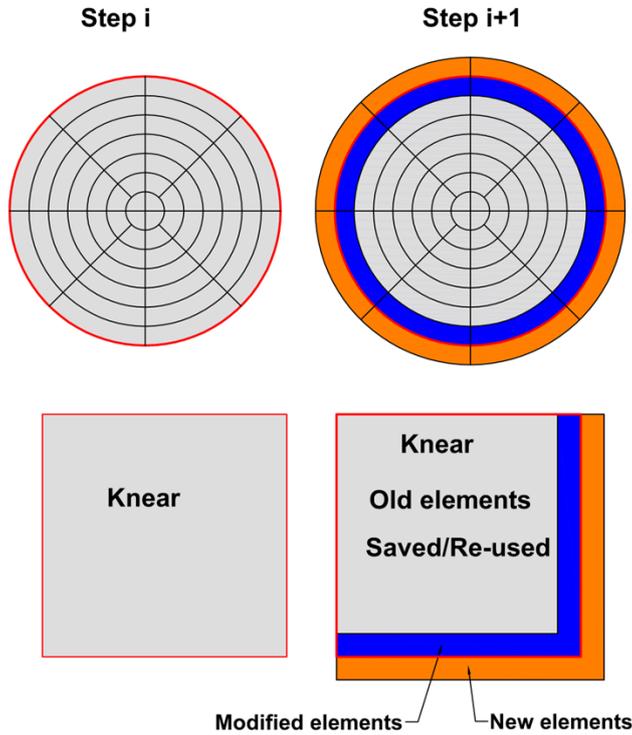
Figure 5: *Efficient* $\mathbf{K}_{near}$ *updating.*

4. Improvements and optimizations

Our multilevel fast multipole SGBEM code extends previous work [24, 19] by implementing the fatigue crack growth treatment described in Sec. 3 together with computational improvements (described next in Secs. 4.1 to 4.3) and the handling of surface-breaking cracks (Sec. 4.4). It is written in Fortran and incorporates algorithms from the BE community such as (i) the singular integration schemes of Andrä and Schnack [35, 6], (ii) the index of severity [36] for adjusting the Gaussian quadrature density to the interelement distance, (iii) the nested flexible GMRES (FGM-RES) which uses $\mathbf{K}_{\mathrm{near}}$ as a preconditioner [18] and (iv) the extension to multizone configurations of the SGBEM [37]. These features and attendant performance enhancements are reported in [24, 19]. Matrix-vector operations are performd using subroutines from the BLAS library. The FGMRES algorithm used is available at *www.cerfacs.fr* and described in [38].

4.1. Efficient update of $\mathbf{K}_{near}$

At each increment, a layer of new elements is added to the mesh and the system (3) must be updated; this in particular requires re-setting the matrix $\mathbf{K}_{\mathrm{near}}$ of near interactions. Recomputing $\mathbf{K}_{\mathrm{near}}$ is wasteful since many of the influence coefficients are equal to those for the previous mesh configuration. Therefore, starting from the second increment, the interactions between pairs of old elements are re-used. Only the parts of the matrix that are related to the newly added or modified elements are computed, see Fig. 5.

Re-using the interactions between pairs of old elements for the computation of $\mathbf{K}_{\mathrm{near}}$ is a simple idea, but one must be sure to retain the same conditions as the initial configuration. For example, the octree structure must be kept fixed during the crack advancement simulation so that any pair of

7

elements initially treated as near or far retain that attribute. Also, quarter-point elements are used at the crack front (Sec. 3.2); they are converted to standard eight-noded elements each time a new row of quarter-point elements is added (Sec. 3.3), so their contribution to $\mathbf{K}_{\text{near}}$ is modified after a propagation increment and cannot be simply re-used. To account for this, the contribution of modified elements are saved in Compressed Sparse Row Format in another matrix, and subtracted from the old $\mathbf{K}_{\text{near}}$. Then those elements are set as new elements so that their new contribution is computed and assembled into the updated $\mathbf{K}_{\text{near}}$. By re-using most of the interactions, the cost of re-constructing $\mathbf{K}_{\text{near}}$ is greatly reduced (90% of time reduction is achieved in some of our simulations) especially for cases with small numbers of cracks.

4.2. Parallelization

Parallelization aims at dividing a computation into mutiple subtasks that can be performed concurrently, thereby reducing the overall elapsed time. Many parallel algorithms exist for the boundary element method, see for example [39, 40, 41, 42]. The goal here is to speed up the existing code by avoiding big changes. To this end, we effect a multiprocessing parallelization by using OpenMP. OpenMP is an application program interface (API) for parallel computing on shared memory architectures, which simplifies writing multi-threaded applications by using compiler directives and library routines. Before parallelization, the sequential code is re-organized to reduce the number of operations. Only the M2M, M2L and L2L operations involved in the computation of far interactions, which are time-consuming, have been parallelized. Simulations done on a 20-core Intel Xeon E5-2630v4 processor running at 2.2 GHz (with 128 Go installed memory) have shown a speedup factor of about 13.0 on the parallelized part.

4.3. Upper bounded incremental coordinate format

In large scale simulations, the memory usage requires close attention, especially in a context of parallel computing. In our code, the compressed sparse row (CSR) format is used for storing the matrices, but a dense format is used for their construction, causing large amounts of allocated but unused memory. Due to parallelization, the dense format causes peaks of allocated memory. To avoid this, an upper bounded incremental coordinate (UBI-COO) format is designed for matrix construction. The coordinate format (COO), which stores each non-zero matrix entry with its coordinates, is well known for setting up sparse matrices. Using dense format is simple: a dense matrix is allocated and is converted to CSR format at the end of the construction. With the UBI-COO, the coordinate format is used in an incremental way. A parameter sets the maximal amount of data in the COO. When the limit is reached, the COO matrix is converted to CSR and the CSR is merged with the existing CSR. At this step, multiples entries are also merged. The COO is then reinitialized for the rest of the construction. Based on Sparsekit subroutines [43], necessary subroutines for the manipulation of the matrices in COO or CSR format are written. This upper bounded incremental coordinate format erases memory peaks in the matrix construction phases.

4.4. Surface-breaking cracks

Surface-breaking cracks (SBCs) are among the critical sources of structural degradation. Their detection and the prediction of their evolution are of great interest in civil engineering. Many investigations have been devoted to SBCs. For example, Raju and Newman [44] provided stress intensity factors by using the FEM, Feng and Hong [45] presented an expression of the surface crack opening displacement in a plate under tension and bending, Frangi [12] used the SGBEM to simulate a surface-breaking crack, Ramezani [46] used the dual BEM to evaluate stress intensity
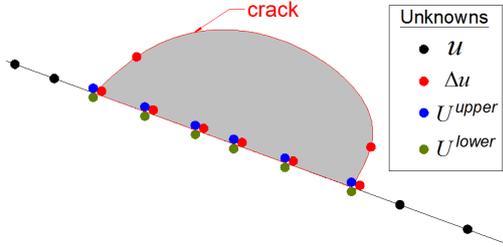
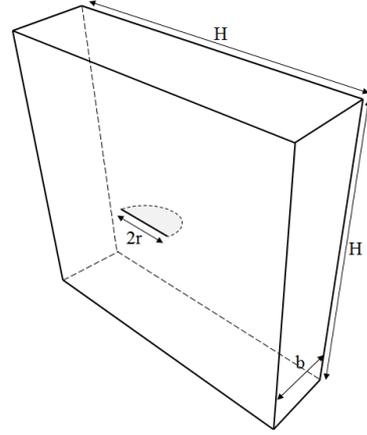**Figure 6:** *Surface-breaking crack: multiple nodal unknowns*

Figure 7: *Surface-breaking crack example: geometry*

factors of surface cracks in round bars. We therefore have included SBC analysis in our code. This mainly requires a proper treatment of the DOFs at nodes on the intersection $S_t \cap S_c$ between the crack and the outer surface (Fig. 6). Each node of this intersection carries three unknowns, namely the displacements $\boldsymbol{u}^{\text{upper}}$ and $\boldsymbol{u}^{\text{lower}}$ of the upper and lower faces of the breaking crack (the node belonging to S_t) and the COD $\boldsymbol{\phi}$ (the node also belonging to S_c), linked by

$$\boldsymbol{\phi} = \boldsymbol{u}^{\text{upper}} - \boldsymbol{u}^{\text{lower}} \tag{7}$$

Such nodes are treated as triple nodes (Fig. 6), and (7) is then used to eliminate one of those unknowns in the SGBEM system (3).

To validate this feature, we consider a semi-circular horizontal edge crack (Fig. 7) of radius r breaking at the center of a plate (whose dimensions are $H \times H \times b$, with $H = 10r, b = 2, 5r$) under tension $\sigma = 1$. The adopted plate and crack dimensions are such that the model reasonably represents an edge crack in an infinite plate. The mesh features 1 395 eight-noded elements (1 200 elements for the plate surface and 195 for the crack, see Fig. 8) and 12 651 DOFs. The tolerance for the iterative solver is set to $\epsilon = 10^{-3}$.

For this example, the difference with respect to an internal crack is that the SIF varies along the crack front, with the maximum value at the surface-breaking point. This variation can be represented in terms of the normalized stress intensity factor (NSIF) given by

$$K_{\text{I}}^{\star}(s) = \frac{K_{\text{I}}}{2\sigma}\sqrt{\frac{\pi}{r}}.$$

In Fig. 9, values of $K_{\text{I}}^{\star}$ computed using the present FM-SGBEM are compared with numerical results by Frangi [12] and with approximate values by Sun and Jin [32] and Anderson [47]. The obtained NSIF based on extrapolation equation 4 (noted Present FM-SGBEM 2pts) agrees within 1% (except at the surface-breaking node) with the computed values of [12] while the NSIF based on equation 5 (noted Present FM-SGBEM 1pt) follows the trend of the curve until the surface-breaking node.

Our FM-SGBEM code accommodates multiple surface-breaking cracks, an important feature for civil engineering applications. To illustrate this, consider two surface-breaking cracks in a plate
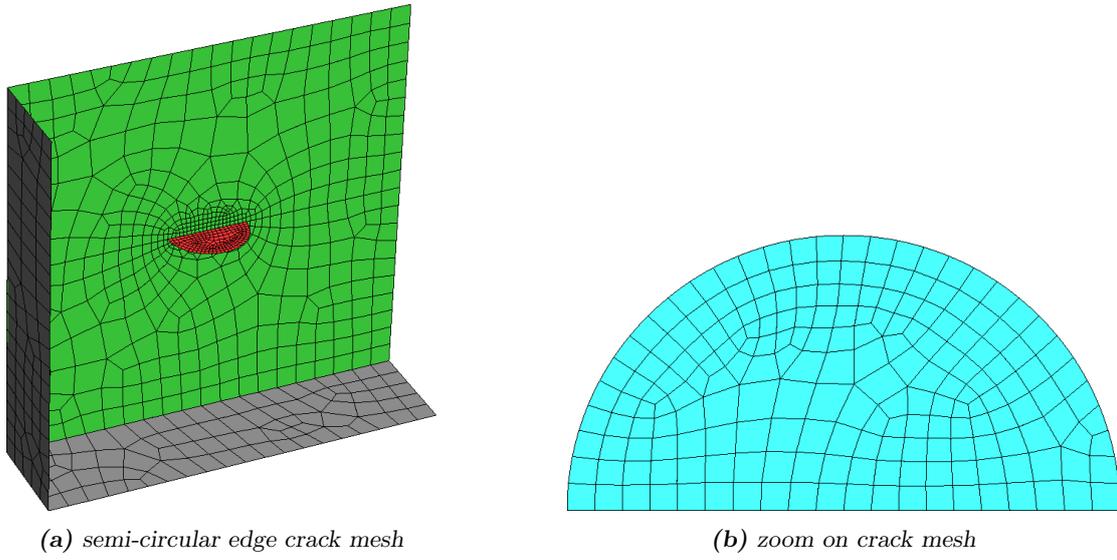
9

(a) *semi-circular edge crack mesh*   **(b)** *zoom on crack mesh*

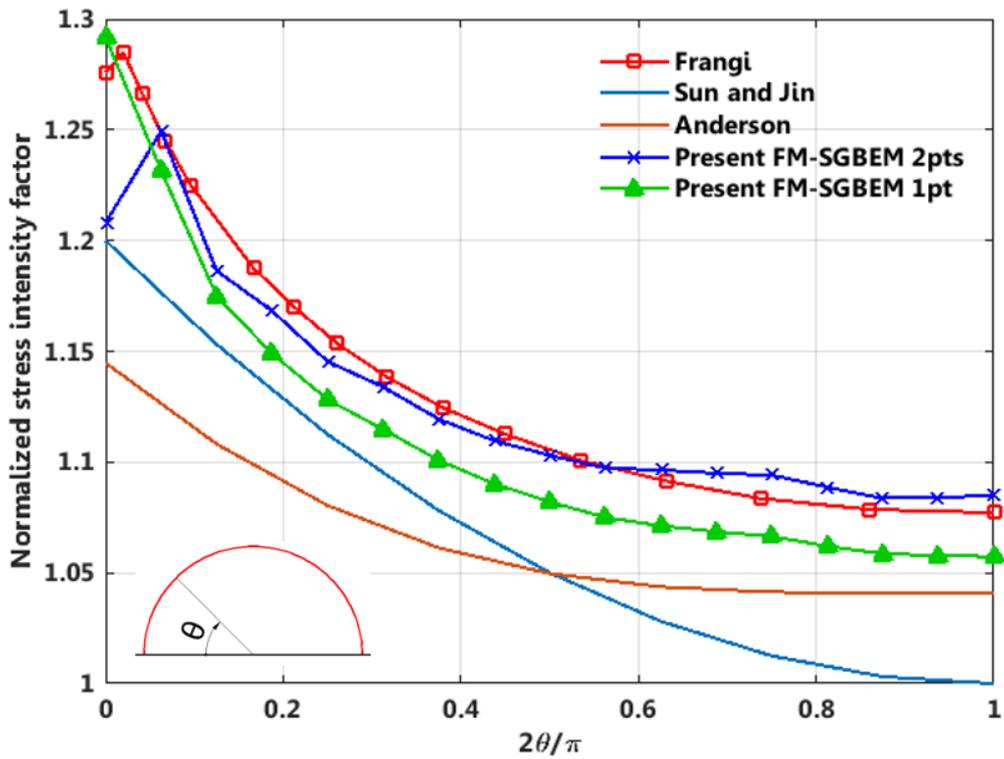**Figure 8:** *Plate with surface-breaking crack: mesh*

Figure 9: *Surface-breaking crack: normalised SIF $K_I^\star$ along the crack front*

(see Fig. 10a, where a part of the surface is removed so that the interior can be seen). Figure 10b presents the COD on the cracks and the vertical displacement on the plate. A zoom on the crack is shown in Fig. 10c. The case of interface-crossing cracks, also very useful, is left to future work.
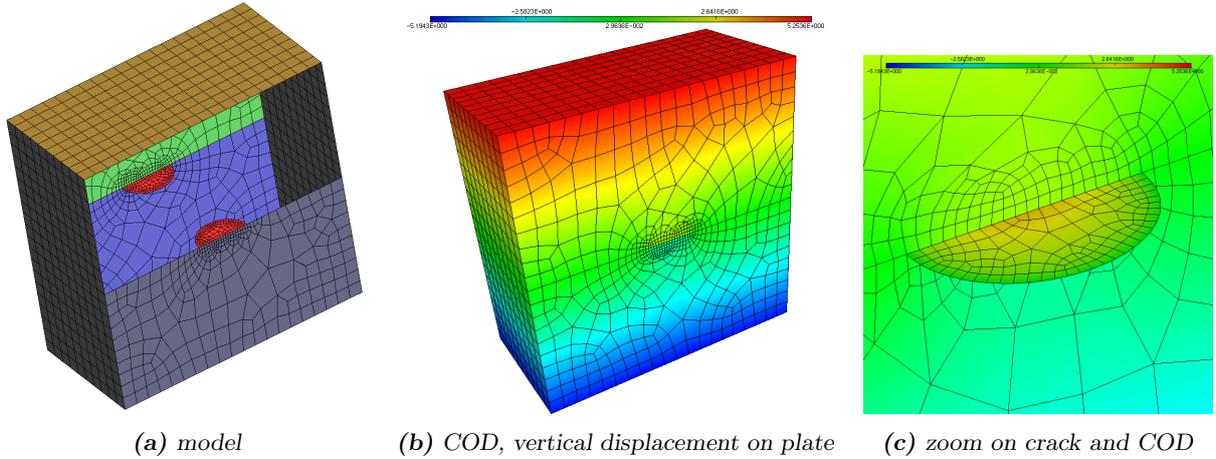
10

(a) model   **(b)** COD, vertical displacement on plate   **(c)** zoom on crack and COD

Figure 10: *Plate with two surface-breaking cracks*

5. Numerical tests: stationary cracks

This section reports numerical tests on configurations involving stationary cracks, all carried out using the previously-described multilevel FM-SGBEM code. The material properties are assumed linear, isotropic, and either homogeneous or (for multizone cases) piecewise homogeneous. The cyclic tensile load is set to a constant amplitude of p. For the FMM procedure, the maximal number of elements in a leaf cell is set to 100 (or 30 for large problems) while the GMRES relative tolerance is $\epsilon = 10^{-3}$. The meshes are created using **Gid**. Outputs are visualized using **Medit**. Eight-noded quadrilateral elements are used to model cracks, with quarter-point elements used along the crack front to better evaluate SIFs. Computing times are measured on an Intel Xeon (20 cores, 2.2 GHz) computer with 128 Go of RAM; however most of the analyses are run sequentially (see sec. 4.2).

In results presented thereafter, T_{pre} is the time needed to compute the right hand-side vector and the coefficients matrix $\mathbf{K}_{\mathrm{near}}$, N_{iter} is the number of outer FGMRES iterations and T_{sol} the corresponding CPU time, T_{tot} is the total CPU time including pre-processing (input reading, octree construction, etc.) and post-processing (results writing in files). The time T_{tot} is compared to the value T_{tot}^{old} achieved with the previous code version [19] by means of the factor

$$\mathrm{SpeedUp} := T_{\mathrm{tot}}^{old}/T_{\mathrm{tot}}.$$

5.1. Homogeneous domain with crack array

In this example, we consider a crack array embedded in a cube (side length 3 m) clamped at its base and subjected to a uniform tensile load $p = 1$ MPa on the top face. The material parameters are $E_1 = 10\,000$ MPa, $\nu_1 = 0.3$. The crack array contains $N_c = n_c^3$ randomly-oriented penny-shaped cracks ($r = 25$ mm) on a cubic grid of step d_c. The center of the crack array coincides with that of the cube. Each crack of the array (see Fig. 11, where the separation d_c is reduced) is meshed with 48 elements and 161 nodes (Fig. 12a), except in simulation 5 for which the crack meshes feature 768 elements and 2 369 nodes (Fig. 12b). The cube and crack arrangements are shown in Fig. 13. Table 1 shows computational data for the corresponding FM-SGBEM analyses.

11

Table 1: *Homogeneous cube with array of stationary cracks: computational data*

#	N_c	N	max_elem	T_{pre} (s)	N_{iter}	T_{sol} (s)	T_{tot} (s)	SpeedUp
1	8	19 302	100	83	24	84	169	**8.7**
2	64	40 974	100	98	41	509	611	**10.5**
3	1 000	403 206	30	1 209	38	2 931	4 478	**16.1**
4	1 728	684 942	30	2 299	39	4 823	8 721	**13.7**
5	1 000	1 075 206	30	3 539	42	6 471	15 446	**10.8**
6	8 000	3 112 206	15	20 160	38	24 840	52 500	**15.9**

5.2. Multizone domain with crack array

The configuration for this example is identical to the previous one except for the fact that the cube is now made of two dissimilar layers ($E_1 = 1\,000$ MPa, $\nu_1 = 0.15$; $E_2 = 2{\times}E_1$ and $\nu_2 = 2{\times}\nu_1$), see Fig. 14. Table 2 shows computational data for FM-SGBEM analyses.

Table 2: *Two-layered cube with array of stationary cracks: computational data*

#	N_c	N	max_elem	T_{pre} (s)	N_{iter}	T_{sol} (s)	T_{tot} (s)	SpeedUp
1	8	17 508	100	79	35	129	209	**7.7**
2	64	39 180	100	205	34	257	465	**14.1**
3	1 000	401 412	30	870	50	3 177	4 497	**11.3**
4	1 728	683 148	30	1 773	44	5 490	8 814	**10.8**
5	2 744	1 061 928	30	2 438	72	17 130	21 498	**9.6**

5.3. 3-layered multicracked road

In this example, we consider N_c rectangular cracks ($3\,000 \times 60$ mm^2) embedded in a portion of three-layered heterogenous road of dimensions $3\,555 \times 3\,300 \times 2\,786$ mm^3, subjected to a wheel load
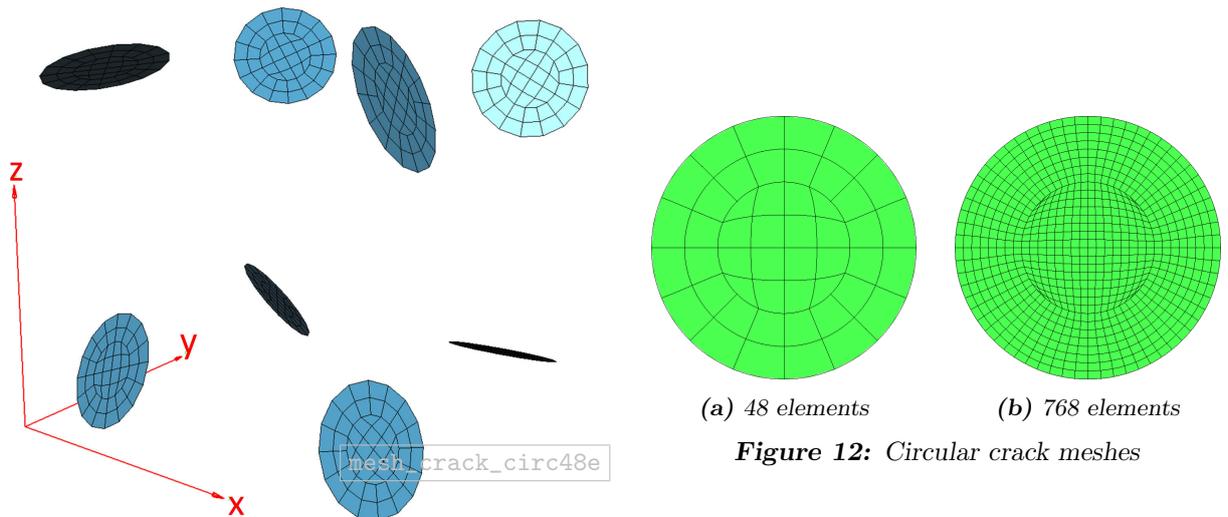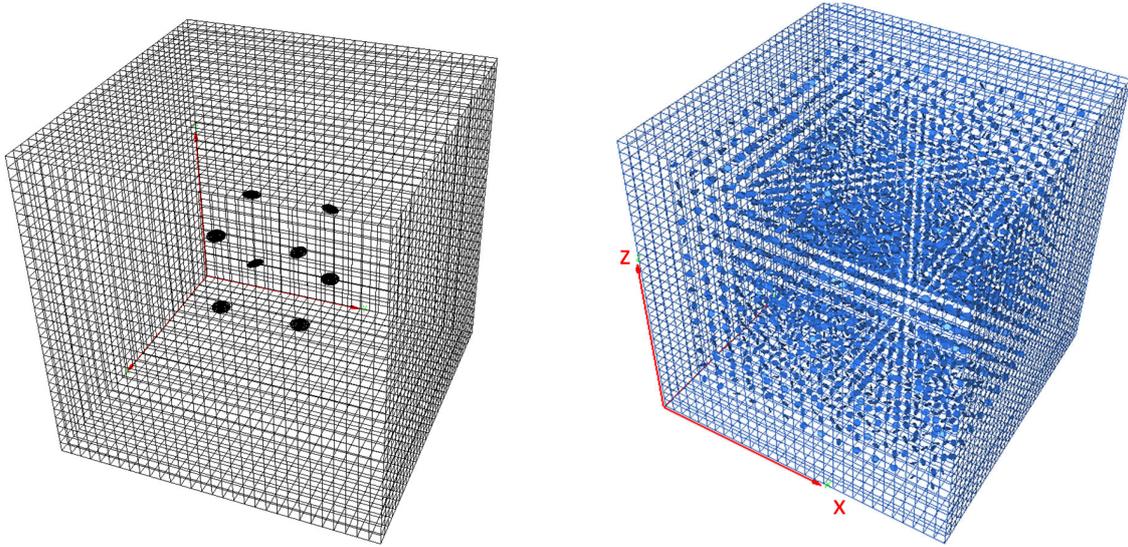

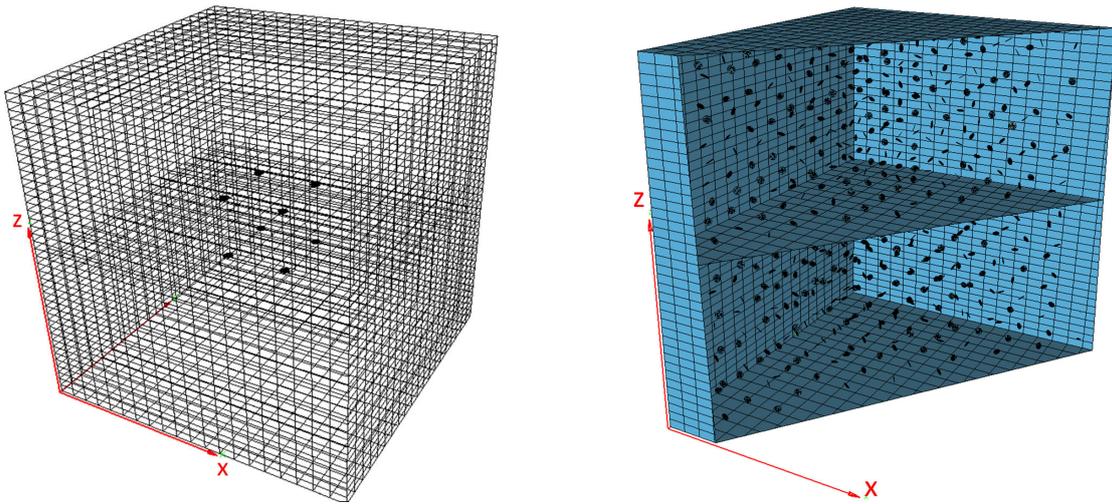**Figure 11:** $2 \times 2 \times 2$ crack array

(a) 48 elements   (b) 768 elements

Figure 12: *Circular crack meshes*

(a) 8 cracks   (b) 2744 cracks

Figure 13: *Homogeneous cube with array of stationary cracks*

(a) 8 cracks   (b) 1000 cracks

Figure 14: *Two-layered cube with array of stationary cracks*

Table 3: *Three-layered road: layer characteristics*

	Thickness (mm)	E (MPa)	ν
Layer 1	66	6610	0,35
Layer 2	500	180	0,3
Layer 3	2220	80	0,25

of $p = 0.6$ MPa at the top face (Fig. 15). The layer characteristics are given in Table 3. The road is meshed with 4 276 four-noded elements and 4 216 nodes, while each crack is meshed with 120
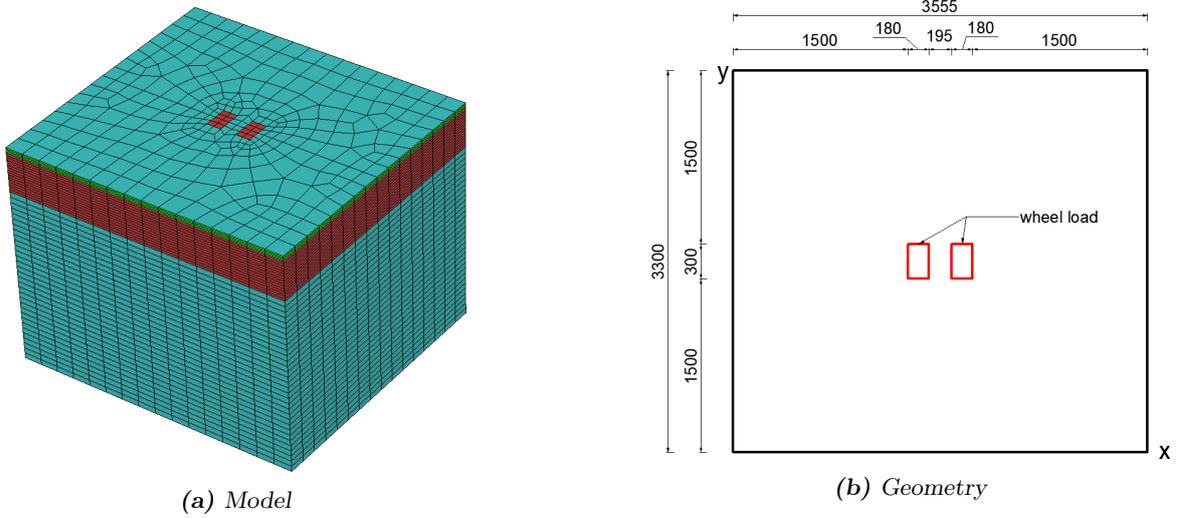
13

(a) *Model*

(b) *Geometry*

Figure 15: *Three-layered road*

Table 4: *Three-layered road with multiple stationary cracks: computational data*

#	N_c	N	max_elem	T_{pre} (s)	N_{iter}	T_{sol} (s)	T_{tot} (s)	SpeedUp
1	1	15 669	500	121	69	283	404	**7.3**
2	3	18 243	500	151	70	355	507	**6.9**
3	7	23 391	500	148	65	366	515	**8.6**
4	15	33 687	500	210	67	635	846	**10.3**
5	30	52 992	500	396	79	1 416	1 813	**13.7**

eight-noded elements and 429 nodes (Fig. 16a). The cracks are embedded in the first, thinnest, layer; their spatial arrangement is shown on Figs 16b,c. Table 4 shows computational data for FM-SGBEM analyses, with N_c ranging from 1 to 30.

6. Numerical tests: fatigue crack propagation

We now present tests on fatigue crack propagation, undertaken under the same conditions as those of Sec. 5. In addition, we denote by N_{init} and N_{end} the number of DOFs for the initial configuration and at the end of the propagation simulation, respectively, while T_{pre}, T_{sol} and T_{tot} are now the preparation, solution and total CPU times, respectively, cumulatively spent for the entire crack growth analysis, i.e. over all growth increments.

6.1. Initially-circular crack in a cylinder

We consider a circular crack of radius $1mm$ in a homogeneous cylinder ($E = 2MPa$, $\nu = 0.3$) of dimensions $R = 60mm$, $H = 120mm$ subjected to tension $\sigma = 2MPa$. The cylinder is meshed with 192 four-noded elements and 194 nodes, while the crack is meshed with 128 eight-noded elements and 417 nodes (Fig. 17a). The material properties for the Paris law are $A = 10^{-8}$ mm/cycle and $m = 4.5$. For this simulation, Δa^{max} is taken equal to $r/10$ and the SIF for a penny-shaped crack in an infinite medium can be used [48]:

$$\Delta K_{\text{I}} = \frac{2}{\pi}\sigma\sqrt{\pi r}, \qquad \Delta K_{\text{II}} = 0.$$

14

(a) Mesh of rectangular crack in (x, z) plane

(b) Positions of rectangular cracks

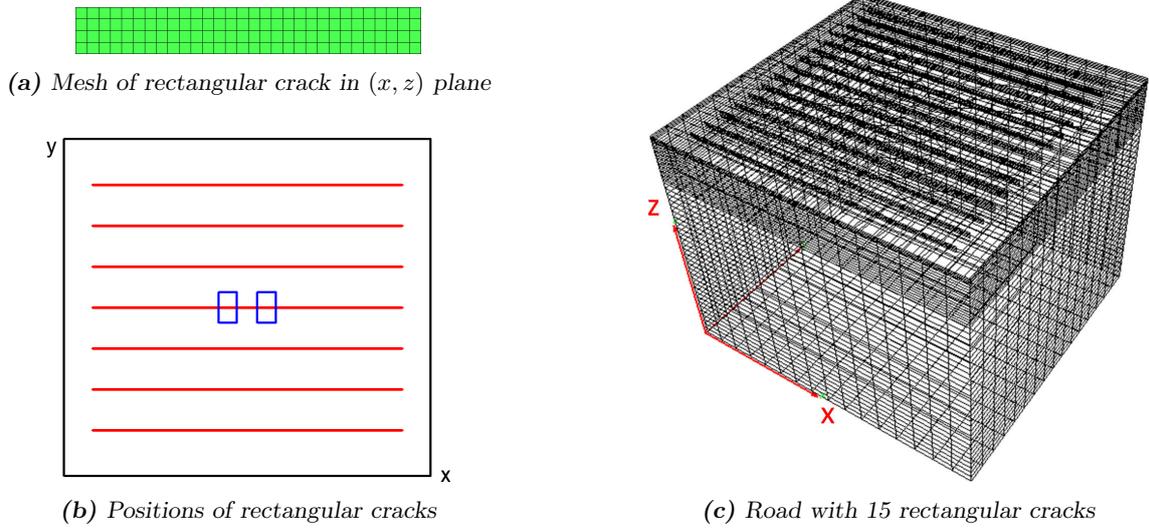(c) Road with 15 rectangular cracks

Figure 16: *Three-layered road with multiple stationary rectangular cracks: arrangement*

The computed fatigue growth (crack radius against number of loading cycles) is plotted in Fig. 17b and compared to the analytic solution derived from the above SIF formulas.

6.2. Multicrack propagation in homogeneous domain

For this example, the initial configuration of the cracked solid is the homogeneous cube-shaped solid with a crack array used in Sec. 5.1. For comparison purpose, the propagation length is taken equal to $r/4$ as the previous version of the code. Table 5 shows computational data for the propagation analyses. The previous version of the code was not run for simulations 3 and 4, as it
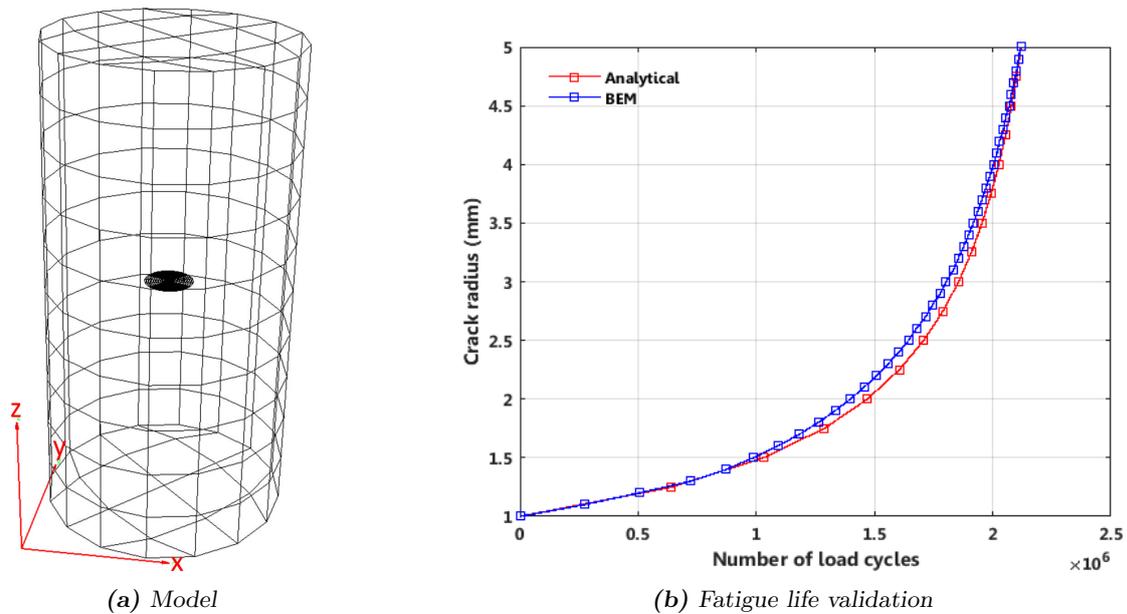

(a) Model

(b) Fatigue life validation

Figure 17: *Cylinder with initially-circular crack*

15

(a) *Propagated 8-crack array*

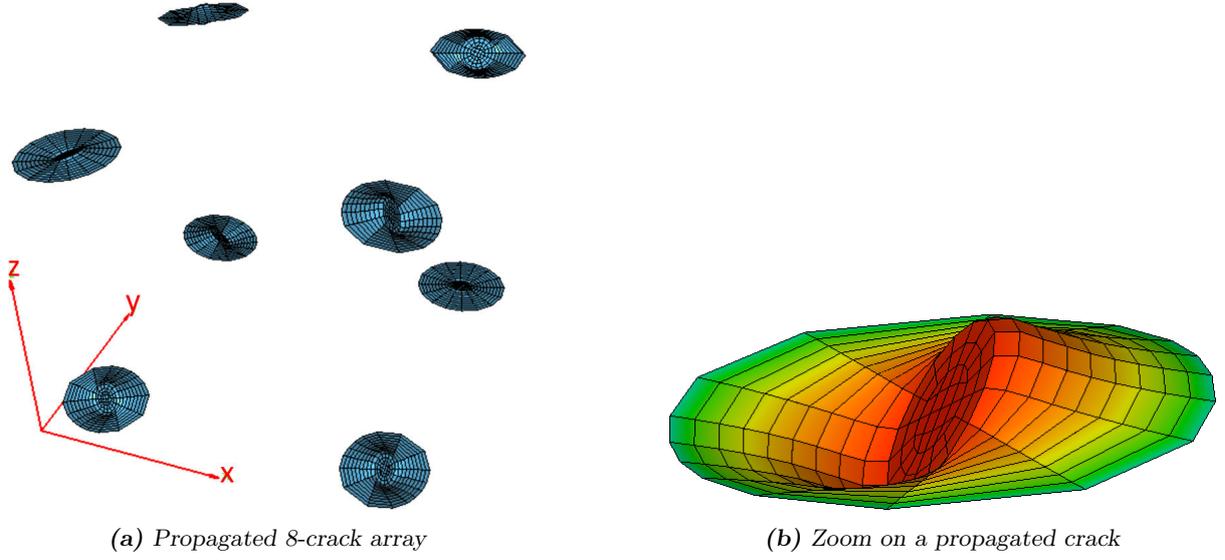**(b)** *Zoom on a propagated crack*

Figure 18: *Multi-crack propagation in homogeneous cube*

would have required too much time. The final shape of the propagated cracks depicted in Fig. 18.

6.3. Multicrack propagation in multizone domain

Our code can also deal with propagation in multizone domain provided cracks do not cross interfaces. For an illustration, we use as initial configuration the cracked two-layered solid of Sec. 5.2 and compute the subsequent fatigue crack propagation. Table 6 shows computational data for the propagation analyses.

6.4. Application: Cracked road

In this application, we consider initially penny-shaped cracks (with radius $r = 10$ mm and the distance $d_c = 250$ mm between them) embedded in the heterogenous road of Sec. 5.3, whose characteristics are again given by Table 3, subjected to a wheel load of $p = 0.6$ MPa (Fig. 15). The crack centers are located on the mid-plane of the first layer (Fig. 19). Fatigue propagation is computed with $N_{\text{cycles}} = 10$ and $\Delta a^{max} = r/4$. The material properties for the Paris law

Table 5: *Homogeneous cube with array of propagating cracks: computational data*

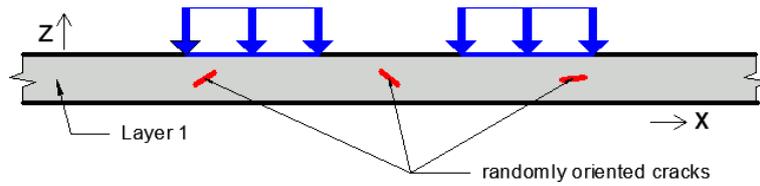| #	N_c	N_{init}	N_{cycles}	N_{end}	T_{pre}	T_{sol}	T_{tot}	SpeedUp
1	8	19 302	10	29 670	398	479	889	**35.3**
2	64	40 974	10	123 918	2 286	5 872	8 217	**52.6**
3	512	199 950	12	1 010 958	22 159	45 158	71 905	—

Figure 19: *Initially penny-shaped cracks in top layer of three-layered road*

16

Table 6: *Multizone Cube with array of propagating cracks: computational data*

#	N_c	N_{init}	N_{cycles}	N_{end}	T_{pre}	T_{sol}	T_{tot}
1	8	17 508	10	27 876	330	599	939
2	64	39 180	10	122 124	2 259	4 907	7 223

Table 7: *Three-layered road with multiple propagating cracks: computational data*

#	N_c	N_{init}	N_{end}	$T_{\text{pre}}(\text{s})$	$T_{sol}(\text{s})$	$T_{\text{tot}}(\text{s})$
1	1	15 441	18 033	201	667	883
2	3	17 559	25 335	345	1 382	1 749
3	5	19 677	32 637	1 241	3 166	4 434

are $A = 10^{-8} mm/cycle$ and $m = 4.5$. Table 7 presents computational data for the propagation analyses. The final shape of the propagated cracks and the crack opening displacement in z direction are shown in Fig. 20 for simulation 1 (one crack) and in Fig. 21 for simulation 2 (three cracks).
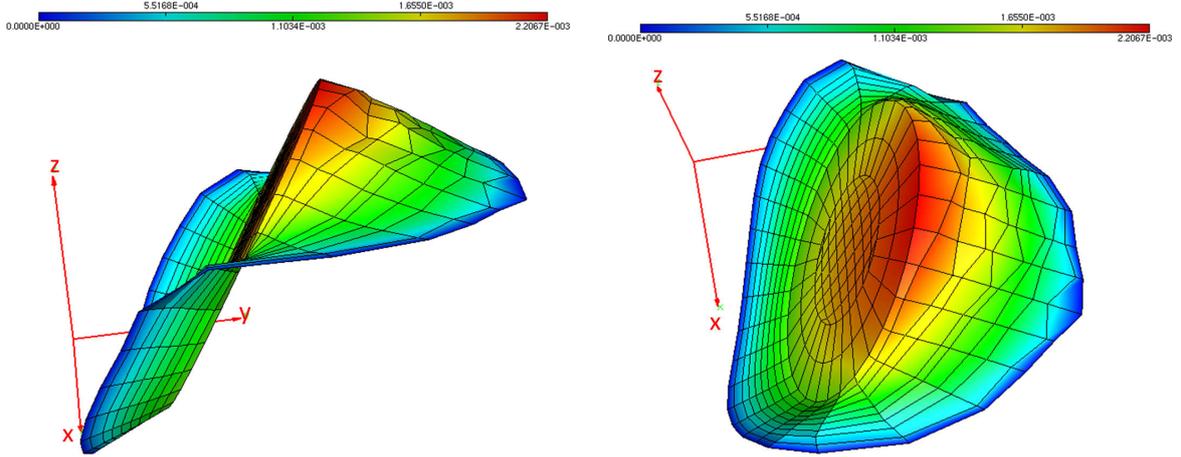

Figure 20: *Propagation of single crack in three-layered road: views from two directions*

7. Conclusion

This research has shown that the fast multipole SGBEM (FM-SGBEM) is able to deal with crack propagation problems in linear fracture mechanics efficiently and fast. The performance of the FM-SGBEM is improved to deal with large-scale multicrack propagation. The method is able to solve million-DOF problems in a few hours on a single workstation. To address realistic applications, more-elaborate propagation criteria will be investigated in future work; moreover, adaptive mesh refinement methods such as that developed in [49] for the BEM can be implemented to control the accuracy of computed solutions. The propagation of surface-breaking cracks and crossing interface cracks will be studied. Thus applications on civil engineering structures will be carried out.
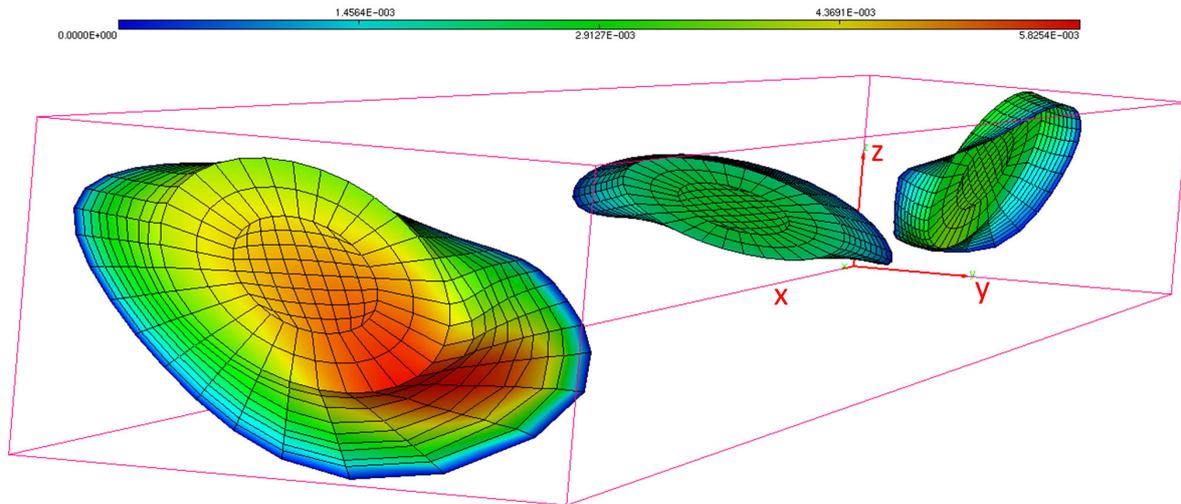
17

Figure 21: *Propagation of multiple cracks in three-layered road: COD in z direction*

References

[1] Sukumar, N., Chopp, D. L., Béchet, E., Moës, N. (2008). Three-dimensional non-planar crack growth by a coupled extended finite element and fast marching method. *Int. J. Num. Meth. Eng.*, **76**:727-748.

[2] Li, X., Keer, L. M. (1992). A direct method for solving crack growth problems-II. Shear mode problems. *Int. J. Solids Struct.*, **29**:2749-2760.

[3] Mi, Y., Aliabadi, M. H. (1994). Three-dimensional crack growth simulation using BEM. *Comput. Struct.*, **52**:871-878.

[4] Mi, Y. (1996). Three-dimensional analysis of crack growth. Computational Mechanics Publications.

[5] Yoshida, K. (2001). Applications of fast multipole method to boundary integral equation method. PhD thesis, Kyoto University, Japan.

[6] Frangi, A., Novati, G., Springhetti, R., Rovizzi, M. (2002). 3D fracture analysis by the symmetric Galerkin BEM. *Comput. Mech.*, **28**:220-232.

[7] Costabel, M. (1987). Symmetrie methods for the coupling of finite elements and boundary elements. In Boundary Elements IX (C. Brebbia, W. Wendland, G. Kuhn, 1, 411-420). Berlin: Springer.

[8] Ganguly, S., Layton, J. B., Balakrishna, C. (2000). Symmetric coupling of multi-zone curved Galerkin boundary elements with finite elements in elasticity. *Int. J. Num. Meth. Eng.*, **48**:633-654.

[9] Springhetti, R., Novati, G., Margonari, M. (2006). Weak coupling of the Symmetric Galerkin BEM with FEM for potential and elastostatic problems. *Comput. Mod. Eng. Sci.*, **13**:67-80.

[10] Sauter, S., Schwab, C. (2011). Boundary element methods. Springer.

[11] Costabel, M., Stephan, E. P. (1987). An improved boundary element Galerkin method for three-dimensional crack problems. *Integ. Equ. Oper. Theory*, **10**:467–504 (1987).

[12] Frangi, A. (2002). Fracture propagation in 3D by the symmetric Galerkin boundary element method. *Int. J. Fract.*, **116**:313-330.

[13] Roberts, D. J., Phan, A.-V., Tippur, H. V., Gray, L. J., Kaplan, T. (2010). SGBEM modeling of fatigue crack growth in particulate composites. *Archive Appl. Mech.*, **80**:307-322.

[14] Kitey, R., Phan, A.-V., Tippur, H. V., Kaplan, T. (2006). Modeling of crack growth through particulate clusters in brittle matrix by symmetric-Galerkin boundary element method. *Int. J. Fract.*, **141**:11-25.

[15] Xu, K., T. Lie, S., Cen, Z. (2004). Crack propagation analysis with Galerkin boundary element method. *Int. J. Numer. Anal. Meth. Geomech.*, **28**:421-435.

[16] Távara, L., Mantič, V., Salvadori, A., Gray, L. J., París, F. (2011). SGBEM for cohesive cracks in homogeneous media. *Key Eng. Mater.*, **454**:1-10.

[17] Greengard, L., Rokhlin, V. (1987). A fast algorithm for particle simulations. *J. Comp. Phys.*, **73**:325–348.

[18] Chaillat, S., Semblat, J. F., Bonnet, M (2012). A preconditioned 3-D multi-region fast multipole solver for seismic wave propagation in complex geometries. *Commun. Comput. Phys.*, **11**:594–609.

18

[19] Trinh, Q. T. (2014). Modelling multizone and multicrack in three-dimensional elastostatic media: a Fast multipole Galerkin Boundary Element Method. PhD Thesis, INSA Strasbourg.

[20] Han, Z., Atluri, S. N. (2002). SGBEM (for cracked local subdomain) - FEM (for uncracked global structure) alternating method for analyzing 3D surface cracks and their fatigue growth. *Comput. Mod. Eng. Sci.*, **3**:699-716.

[21] Nikishkov, G., S. N. Atluri, S. (2002). Combining SGBEM and FEM for modeling 3D cracks. In Engineering Computational Technology (B.H.V. Topping and Z. Bittnar, 167-192). Saxe-Coburg.

[22] Bonnet, M. (1999). Boundary integral equation methods for solids and fluids. Wiley.

[23] Pham, D., Mouhoubi, S., Bonnet, M., Chazallon, C. (2012). Fast multipole method applied to symmetric Galerkin boundary element method for 3D elasticity and fracture problems. *Eng. Anal. Bound. Elem.*, **36**:1838-1847.

[24] Trinh, Q. T., Mouhoubi, S., Chazallon, C., Bonnet, M. (2015). Solving multizone and multicrack elastostatic problems: A fast multipole symmetric Galerkin boundary element method approach. *Eng. Anal. Bound. Elem.*, **50**:486-495.

[25] Li, S., Mear, M. E., Xiao, L. (1998). Symmetric weak-form integral equation method for three-dimensional fracture analysis. *Comp. Meth. Appl. Mech. Eng.*, **151**:435–459.

[26] Rooke, D. P. (1976). Compendium of stress intensity factors. H.M. Stationery Office. London.

[27] Aliabadi, M. H., Rooke, D. P., Cartwright, D. J. (1987). An improved boundary element formulation for calculating stress intensity factors: Application to aerospace structures. *J. Strain. Anal. Eng. Des.*, **22**:203–207.

[28] Barsoum, R. S. (1974). On the use of isoparametric finite element in linear fracture mechanics. *Int. J. Num. Meth. Eng.*, **10**:25–37.

[29] Paris, P., Erdogan, F. (1963). A critical analysis of crack propagation laws. *J. Basic Eng.*, **85**:528-533.

[30] Bouchard, P.O., Bay F., Chastel Y. (2003). Numerical modeling of crack propagation: automatic remeshing and comparison of different criteria. *Comput Methods Appl Mech Eng*, **192**:3887–3908.

[31] Ma, S. (2005). Propagation de fissure en mode mixte dans un milieu élasto-plastique avec prise en compte des contraintes résiduelles. PhD Thesis, Université Blaise Pascal - Clermont Ferrand II, France.

[32] Sun, C.T., Jin Z.-H. (2012). Fracture Mechanics. Academic Press.

[33] Recho, N. (2012). Fracture Mechanics and Crack Growth. Wiley.

[34] Erdogan, F., Sih, G. C. (1963). On the crack extension in plates under plane loading and transverse shear. *J. Basic Eng.*, **85**:519-525.

[35] Andrä, H., Schnack, E. (1997). Integration of singular Galerkin-type boundary element integrals for 3D elasticity problems. *Numerische Mathematik*, **76**:143-165.

[36] Rezayat, M., Shippy, D. J., Rizzo, F. J. (1986). On time-harmonic elastic-wave analysis by the boundary element method for moderate to high frequencies. *Comp. Meth. Appl. Mech. Eng.*, **55**:349-367.

[37] Gray, L. J., Paulino, G. H. (1997). Symmetric Galerkin boundary integral formulation for interface and multi-zone problems. *Int. J. Num. Meth. Eng.*, **40**:3085-3101.

[38] Fraysse, V., Giraud, L., Gratton, S. (1998). A set of Flexible-GMRES routines for real and complex arithmetics. Technical Report TR/PA/98/20, CERFACS.

[39] Greengard, L., Gropp, W. D. (1990). A parallel version of the fast multipole method. *Comput. Math. Appl.*, **20**(7):63-71.

[40] Adelman, R., Gumerov, N., Duraiswami, R. (2017). FMM/GPU-accelerated boundary element method for computational magnetics and electrostatics. *IEEE Trans. Magn.*, **53**:1-11.

[41] Gu, J., Zsaki, A. M. (2018). Accelerated parallel computation of field quantities for the boundary element method applied to stress analysis using multi-core CPUs, GPUs and FPGAs. *Cogent Eng.*, **5**:1-21.

[42] Ptaszny, J. (2018). Parallel fast multipole boundary element method applied to computational homogenization. AIP Conference Proceedings, 1922(1), 140003.

[43] Saad, Y. (1990). SPARSKIT, a basic tool kit for sparse matrix computations (Technical Report No. 1029). Center for Supercomputing Research and Development, University of Illinois at Urbana-Chanpaign.

[44] Raju, I. S., Newman, J. C. (1979). Stress-intensity factors for a wide range of semi-elliptical surface cracks in finite-thickness plates. *Eng. Fract. Mech.*, **11**:817-829.

[45] Feng, D.-Z., Hong, Q.-C. (1992). Investigation of surface crack opening displacement and its application in pressure vessels and piping. *Int. J. Pressure Vessels Piping*, **52**:227-239.

[46] Ramezani, M. K., Purbolaksono, J., Andriyana, A., Ramesh, S., Mardi, N. A. (2018). Analysis of surface cracks in round bars using dual boundary element method. *Eng. Anal. Bound. Elem.*, **93**:112-123.

[47] Anderson, T.L. (2005). Fracture Mechanics: Fundamentals and Applications. Taylor and Francis Group.

[48] Williams, M.L. (1957). On the stress distribution at the base of a stationary crack. *J. Appl. Mech.*, **24**:109-114.

[49] Chaillat, S., Groth, S., Loseille, A. (2018). Metric-based anisotropic mesh adaptation for 3D acoustic boundary element methods. *J. Comput. Phys.*, **372**:473-499.

19